ADVANCED ELECTRONIC MATERIALS Open Access
www.advelectronicmat.de

Freestanding Membranes of Titania Nanorods, Photocatalytically Reduced Graphene Oxide, and Silk Fibroin: Tunable Properties and Electrostatic Actuation

*Finn Dobschall, Hauke Hartmann, Sophia Caroline Bittinger, Norbert Schulz, Hendrik Schlicke, Hoc Khiem Trieu, and Tobias Vossmeyer**

In this study, the mechanical properties of freestanding membranes made of graphene oxide (GO), titania nanorods (TNRs), and silk fibroin (SF) are investigated and their application is demonstrated as electrostatically driven actuators. Using a stamping process, the membranes are transferred onto substrates with circular apertures or square cavities measuring ~80 to 245 µm in diameter or edge length, respectively. Afterwards, the membranes are exposed to deep-UV (DUV) radiation in order to photocatalytically convert GO to reduced graphene oxide (rGO). Microbulge tests combined with atomic force microscopy (AFM) measurements reveal enhanced mechanical stability after the DUV treatment, as indicated by an increase of Young's modulus from ~22 to ~35 GPa. The toughness of the DUV-treated membranes is up to ~1.25 MJ m^{-3}, while their ultimate biaxial tensile stress and strain are in the range of ~377 MPa and ~0.68%, respectively. Further, by applying voltages of up to ±40 V the membranes are electrostatically actuated and deflected by up to ~1.7 µm, as determined via in situ AFM measurements. A simple electrostatic model is presented that describes the deflection of the membrane as a function of the applied voltage very well.

1. Introduction

Conventional micro- and nanoelectromechanical systems (MEMS/NEMS) are usually made from silicon using advanced lithographic methods. In recent years, however, numerous studies have explored the fabrication of MEMS/NEMS from nanomaterials to enable tunable functional properties beyond those of purely silicon-based devices.[1,2] For example, 2D-nanomaterials and nanoparticle-based freestanding membranes have been used for the fabrication of highly sensitive pressure sensors,[3,4] electrostatic actuators,[5,6] resonators,[7,8] and chemical sensors.[9,10] Furthermore, such hybrid devices can be fabricated using print methods, such as transfer printing.[11] However, in order to use nanomaterials for such applications, they must be robust enough. Additionally, a fundamental knowledge of their mechanical and electromechanical properties is indispensable to enable their rational implementation into hybrid MEMS/NEMS for specific applications.

The mechanical properties of substrate-supported thin films are commonly studied by nanoindentation tests.[12,13] However, this method has a lower limit on the film thickness, which should exceed ~10 times the indentation depth to avoid interference from the substrate. As an alternative approach, microbulge tests have been used to probe the mechanical properties of freestanding membranes from different materials, such as carbon nanosheets,[14] titania nanocrystals (TNCs),[15] and gold nanoparticles.[16] Using bulge experiments, the elastic

The ORCID identification number(s) for the author(s) of this article can be found under https://doi.org/10.1002/aelm.202400602

[+]Present address: CIC biomaGUNE, Basque Research and Technology Aliance (BRTA), Donostia-San Sebastian 20014, Spain

[++]Present address: Nexperia Germany, Stresemannallee 101, 22529 Hamburg, Germany

[+++]Present address: Institute of Physical Chemistry and Polymer Physics, Leibniz Institute of Polymer Research Dresden, Hohe Strasse 6, 01069 Dresden, Germany

DOI: 10.1002/aelm.202400602

F. Dobschall, H. Hartmann, S. C. Bittinger[+], T. Vossmeyer
Institute of Physical Chemistry
University of Hamburg
Grindelallee 117, 20146 Hamburg, Germany
E-mail: tobias.vossmeyer@chemie.uni-hamburg.de
N. Schulz[++], H. K. Trieu
Institute of Microsystems Technology
Hamburg University of Technology
Eißendorfer Str. 42, 21073 Hamburg, Germany
H. Schlicke[+++]
Fraunhofer Center for Applied Nanotechnology CAN
Grindelallee 117, 20146 Hamburg, Germany

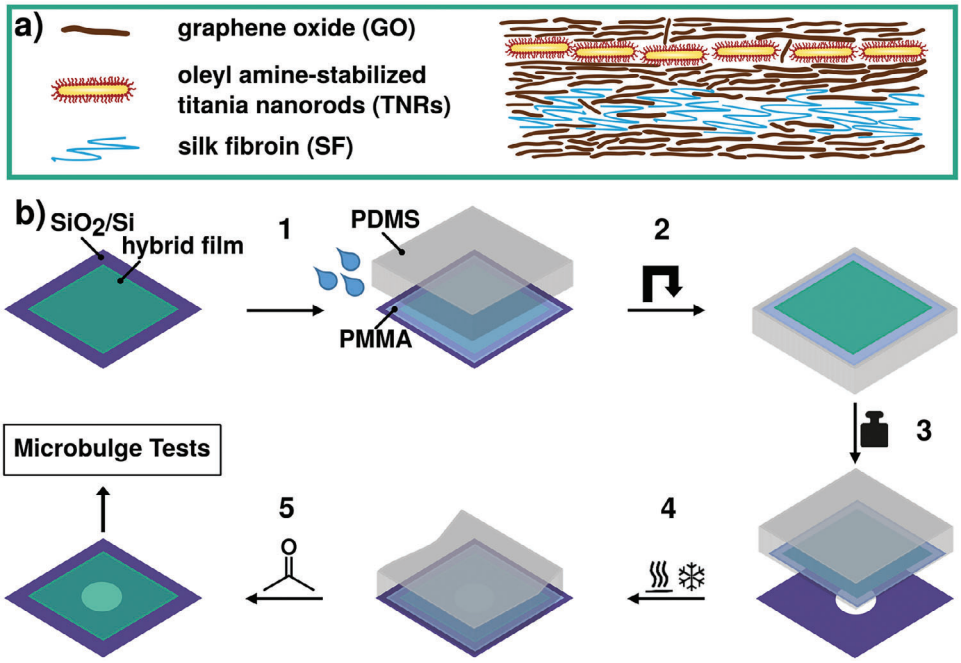

Figure 1. Schematic of (a) the hybrid film consisting of GO, TNRs, and SF and (b) the fabrication process of the freestanding membranes. Step 1: dissolving the sacrificial PVA layer at the film/substrate interface with water and placing the PDMS stamp (transparent grey) onto the hybrid film (green) which is protected by a PMMA top layer (light blue). Step 2: removing the stamp with the hybrid film protected by the PMMA layer. Step 3: placing stamp on target silicon substrate with aperture and applying pressure. Step 4: heating and cooling cycles to completely detach the film from the PDMS stamp. Step 5: dissolving the protective PMMA layer in acetone after removing the PDMS stamp. The mechanical properties of the obtained membrane can now be studied via AFM microbulge tests.

properties are sampled non-destructively over a larger area compared to local nanoindentation tests. In a recent study, we applied microbulge tests to measure the elastic properties of crosslinked gold nanoparticle membranes.[17] Besides, we demonstrated applications of freestanding gold nanoparticle membranes as highly sensitive resistive pressure gauges[18] and electrostatic actuators.[6] Drawbacks of these membranes are their limited mechanical stability and susceptibility to oxidation.

Freestanding membranes from graphene-based materials feature promising mechanical properties, including high strength and toughness.[19,20] Further, composites of graphene oxide (GO) and biomaterials have been prepared to combine their respective mechanical stability and flexibility. For instance, Tsukruk and co-workers fabricated ultra robust GO/cellulose membranes[21] and GO/silk fibroin (SF) membranes[22] by depositing the different components alternatingly via spin coating. For the fabrication of the GO/cellulose composites, they used rod-shaped cellulose nanocrystals resulting in a maximum toughness of 3.9 MJ m^{-3} for a GO content of 59.1 wt%. In the case of the GO/SF composites increasing volume fractions of GO were incorporated into the SF matrix resulting in a maximum toughness of 2.4 MJ m^{-3} at 23.5 vol% GO.

In general, the mechanical properties of graphene/GO membranes depend significantly on their chemical functionalization and crosslinking to other nanomaterials. GO exposes numerous carboxy and hydroxyl groups and, hence, it is expected to show good affinity to the surface of TNCs.[23] Further, TNCs are known to reduce GO to reduced graphene oxide (rGO) in solution as well as in films[24,25] under UV irradiation based on their photocatalytic activity. Here, we used a stamping method to fabricate freestanding membranes composed of titania nanorods (TNRs), GO, and SF (TNR/GO/SF).[11] The incorporation of TNRs into the composite membranes enabled the facile and well-controlled photocatalytic reduction of GO via exposure to deep-UV (DUV) irradiation. The effect of the DUV treatment on the mechanical properties was probed via atomic force microscopy (AFM) bulge tests. Furthermore, the formation of rGO during DUV treatment induced electrical conductivity and enabled the electrostatic actuation of the resulting freestanding TNR/(rGO/GO)/SF membranes.

2. Results and Discussion

2.1. Fabrication of Freestanding Hybrid Membranes

The hybrid films investigated in this study were fabricated from dispersions of graphene oxide (GO), titania nanorods (TNRs), and silk fibroin (SF) via layer-by-layer spin-coating (LbL-SC).[11,22] Exemplary transmission electron microscopy (TEM) and atomic force microscopy (AFM) images of the TNRs and GO flakes are shown in the Supporting Information, Section S1. The multilayered structure of the hybrid films is schematically shown in **Figure 1a**. Considering the well-known binding of carboxylate groups to titania surfaces,[15,23] it is expected that TNRs can easily be compounded with GO.[26,27] For example, Hug et al. demonstrated the dissociative adsorption of various carboxylic acids on a clean titania surface using Fourier-transform infrared

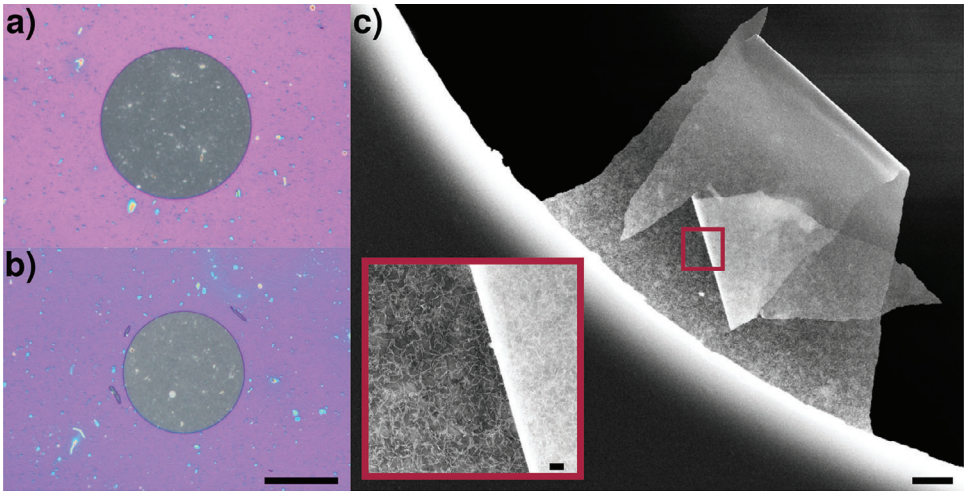

Figure 2. Optical micrographs of freestanding hybrid membranes M1 (a) and M2 (b) taken before the DUV exposure. The membranes span circular apertures with diameters of ~105 µm (M1) and ~84 µm (M2). Scale bar: 50 µm. (c) SEM image of hybrid membrane M1 after a burst test. Scale bar: 2 µm. The inset shows the red framed section in higher magnification. Scale bar: 200 nm.

(FTIR) spectroscopy,[28] and Ayissi et al. reported a high binding energy for the interaction of titania with carboxylic acid functionalized graphene using density functional theory (DFT).[29] This material combination enables the accelerated photocatalytic reduction of GO to reduced graphene oxide (rGO) using photogenerated charge carries produced by the TNRs under illumination with deep ultraviolet (DUV) light.[24,26] Further, SF was integrated into the composite to increase the stability of the film by the formation of hydrogen bonds, polar interactions, and $\pi - \pi$ stacking between GO and SF.[22] GO was used as the overall matrix material while the TNRs were incorporated in the top layers of the hybrid films to provide photocatalytic activity close to the top surface region of the membranes. Spatially separated from the TNRs, the SF was incorporated into the lower layers of the hybrid film to prevent its photocatalytic degradation during DUV exposure. The transfer of the films onto substrates with apertures or cavities was based on a stamping procedure (Figure 1b), which was previously used for the fabrication of freestanding membranes from cross-linked gold nanoparticles and SF/GO composites.[11] A detailed scheme for the fabrication of the freestanding TNR/GO/SF membranes can be found in the Supporting Information, Section S2. In order to facilitate the transfer of the hybrid films from the initial silicon substrate onto the polydimethylsiloxane (PDMS) stamp, the undermost layer of the film consisted of GO. Further, to enable the fabrication of the freestanding membranes, the hybrid films were sandwiched between two polymer layers: a sacrificial layer of polyvinyl alcohol (PVA) underneath and a protective layer of poly(methyl methacrylate) (PMMA) on top of the hybrid films. After removing the top PMMA layer along the edges of the substrate, the sacrificial PVA layer was dissolved by applying a small amount of water to the rim of the film, which was quickly dragged into the film/substrate interfacial region (Figure 1b, Step 1). By gently pressing the PDMS stamp against the substrate, the hybrid film detached from the substrate and was transferred onto the stamp (Figure 1b, Steps 1 and 2). By pressing the stamp against the target substrate, the hybrid film was transferred and freestanding membranes were obtained spanning the cavities or through hole of the substrate (Figure 1b, Step 3). When removing the stamp, the hybrid film must completely detach from the stamp. This was achieved by applying three heating and cooling cycles (Figure 1b, Step 4). Since the thermal expansion coefficients of the PDMS and the substrate-supported PMMA-protected hybrid film differ, the adhesion between the PDMS and PMMA was released, allowing the stamp to be removed from the hybrid film.[30] Finally, the protective PMMA layer was dissolved by immersing the sample in acetone (Figure 1b, Step 5). Before removing the sample from the container, the acetone was exchanged for methoxyperfluorobutane (MPFB). Since MPFB has a lower surface tension than acetone, the solvent exchange prevents rupturing of the membrane when removing the sample from the liquid phase and drying it at ambient conditions.[31] Using this transfer process, it was possible to prepare hybrid membranes with freestanding areas of up to $\sim 6 \times 10^4$ µm^2. The thickness of the as-prepared freestanding membranes was typically between ~25 and ~30 nm, as indicated by AFM height profiles measured at the step edges of intentionally made scratches. Exemplary AFM images of the transferred hybrid films are provided in the Supporting Information, Section S2.

Optical micrographs of freestanding membranes (M1, M2) spanning circular apertures with a diameter of ~105 µm and ~84 µm are shown in **Figure 2**a,b. These membranes were used for the AFM bulge tests presented below. The optical micrographs reveal a fairly homogeneous morphology of the hybrid membranes. Bright spots, however, indicate the deposition of TNR aggregates. Figure 2c shows the SEM images of the remaining parts of a hybrid membrane after a burst experiment (see below). These images clearly reveal the different textures of the bottom and the top surface of the freestanding membrane. On the top surface the morphology is characterized by the TNRs covered with GO sheets while the first deposited layers of GO/SF form a smooth bottom surface. The higher magnification inset indicates

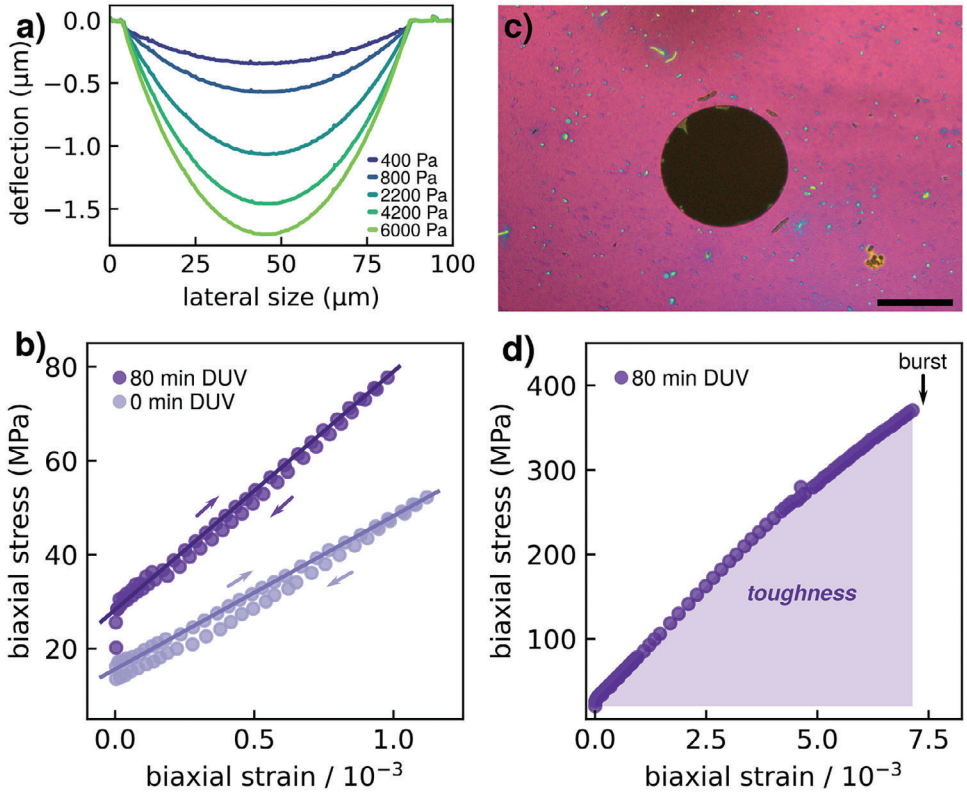

Figure 3. Probing the mechanical properties of membrane M2. (a) Baseline-corrected AFM line scans recorded at different pressures during a bulge test on the TNR/GO/SF membrane before DUV exposure. (b) Stress-strain curves of the hybrid membrane before (light purple) and after 80 min DUV treatment (purple) with linear curve fits to the data acquired in the direction of ascending pressure. (c) Optical micrograph of the substrate after the burst test. Scale bar: 50 µm. (d) Corresponding stress-strain curve of the burst test. The area underneath the graph represents the membrane's toughness.

a rather homogeneous distribution of TNRs in the upper layers of the hybrid membrane.

2.2. Mechanical Properties

In order to characterize the mechanical properties of the hybrid membranes, AFM bulge tests were conducted, similar as described in previous studies.[14,15,17,32] **Figure 3**a shows exemplary bulge profiles of membrane M2. By reducing the pressure underneath the substrate, the membrane was bulged into the aperture. With increasing differential pressure, the deflection of the membrane increased up to ~1.8 µm for the maximum differential pressure of 6 kPa. The biaxial modulus of the membranes was determined by fitting a spherical cap to the bulge profiles for each applied pressure setting, as described previously.[4] By approximating the bulged membrane as part of a thin-walled spherical pressure vessel, the biaxial stress σ can be approximated using the following equation:

$$\sigma = \frac{PR_c}{2t_m} \tag{1}$$

Here, R_c is the radius of the spherical cap, which was extracted as fit parameter, P is the applied pressure, and t_m is the thickness of the freestanding membrane. This approximation is valid for $t_m \ll R_c$, a condition that was met in all our experiments. Further, R_c was used to calculate the full arc length s of the bulged membrane at different pressures:

$$s = 2R_c \arcsin\frac{a}{R_c} \tag{2}$$

Here, a is the aperture radius. The biaxial strain ε experienced by the membrane was then calculated using the following equation:

$$\varepsilon = \frac{s}{2a} - 1 \tag{3}$$

Finally, the stress–strain data were plotted as shown in Figure 3b for, both, ascending and descending pressure. In the elastic regime the correlation between the stress-strain data can be described by the following equation:

$$\sigma = Y\varepsilon + \sigma_0 \tag{4}$$

Here, σ_0 is the membrane's prestress. The biaxial modulus Y was extracted as the slope of the linear function fitted to the data with ascending pressure values (Figure 3b). Comparing the stress-strain data in Figure 3b for ascending and descending pressure reveals only minor hysteresis indicating little deviation from purely elastic behavior. In agreement with previous studies on other types of nanocomposite membranes, we

Table 1. Properties of the membranes M1 and M2 before and after DUV exposure for 80 min. t_m is the thickness, Y is the biaxial modulus, E is the Young's modulus, σ_0 is the prestress, $\sigma_{ultimate}$ is the biaxial ultimate stress, $\epsilon_{ultimate}$ is the biaxial ultimate strain, and U_T is the toughness.

Sample	t_m [nm]	Y [GPa]	E [GPa]	σ_0 [MPa]	$\sigma_{ultimate}$ [MPa]	$\epsilon_{ultimate}$ [%]	U_T [MJ m^{-3}]
M1	26.9	34.5	23.1	13.7	–	–	–
M2	29.5	32.6	21.8	15.6	–	–	–
M1DUV	17.3	56.3	37.5	34.9	383.2	0.64	1.13
M2DUV	21.0	50.9	33.9	28.3	370.4	0.71	1.25

attribute this deviation to retarded elastic deformation and pure viscous creep.[33] Figure S6 (Supporting Information, Section S3) presents the stress-strain characteristics of membrane M1 and confirms that the two membranes M1 and M2 had very similar elastic properties. The mechanical data of both membranes are presented in **Table 1**. For both membranes the biaxial modulus Y was ~33 GPa. Using a Poisson ratio of 0.33,[34,35] this value translates into a Young's modulus of $E = Y(1 - \nu)$ ~22 GPa. Comparable results have been reported by Cho et al., who measured a Young's modulus for GO/SF composite films of 22 GPa using a nanoindentation method.[36] Further, Hu et al. conducted bulge and buckling tests on GO/SF membranes and reported increasing values of Young's modulus from ~10 GPa to ~145 GPa with increasing fractions of GO, ranging from 0 to 23.5 vol%. Comparable to our findings, they measured a modulus of ~25 GPa at a GO volume fraction of ~3%.[22] For comparison, Suk et al.[37] reported Young's moduli of up to ~207 GPa for pure GO monolayers. For pure SF, Young's moduli ranging from 4 to 22 GPa have been reported.[38,39] Additionally, we reported a Young's modulus of ~5 GPa for membranes from TNRs, which were crosslinked by 1,12-dodecanedioc acid.[15]

By DUV exposure GO is photocatalytically reduced to rGO.[25] In addition, the photocatalytic activity of titania triggers the formation of radicals as demonstrated by Soria et al. using electron spin resonance (ESR).[40] Thus, various reactions can be initiated, e.g., radical polymerization and cross-linking in organic materials.[41–43] Hence, we studied how the photocatalytic activity of TNRs can be used to adjust the mechanical properties of TNR/GO/SF membranes. After 80 min DUV exposure the AFM bulge tests were repeated revealing a significantly increased stiffness for both membranes (cf. Figure 3b; Figure S6b, Supporting Information). As seen by the values presented in Table 1, the Young's modulus of both membranes increased to ~35 GPa. In addition, the membranes' prestress increased from ~15 to ~32 MPa. We attribute the enhanced mechanical properties to photocatalytically induced cross-linking between the different components of the membranes. For comparison, Hu et al.[44] reported an increase in the mechanical strength of GO/SF biopapers upon electrochemical microstamping caused by the reduction of GO and the cross-linking of the SF. Further, upon DUV exposure the thickness of the membranes decreased from ~28 to ~19 nm (cf. Table 1; Figure S4, Supporting Information). This observation suggests a significant compaction of the membrane material due to cross-linking. The loss of material is possible due to the formation of volatile reaction products during DUV irradiation.

In order to measure the ultimate stress, strain, and toughness of the membranes, burst experiments were conducted on the DUV-treated samples. Figure 3c shows an optical micrograph of the substrate with only few remains of the membrane M2 at the edge of the aperture after the burst test. The corresponding stress-strain curve is shown in Figure 3d. For membrane M1, the corresponding data are presented in Figure S6 (Supporting Information, Section S3). During the burst experiments, the pressure was increased until the membranes ruptured, defining the ultimate biaxial tensile stress and strain. The corresponding values of the two membranes were very similar (Table 1). The mean values were ~377 MPa and 0.68%, respectively. Further, the membranes' toughness was determined as the area underneath the stress–strain curve, as indicated in Figure 3d. The toughness values for both membranes are presented in Table 1. The corresponding mean value was ~1.2 MJ m^{-3}. For comparison, Hu et al.[22] reported a toughness of ~1.5 MJ m^{-3} for GO/SF membranes with a GO fraction of ~11.5 vol%.

2.3. Electrostatic Actuation

Actuators based on thin membranes find applications in microelectromechanical systems (MEMS), as optical devices, and sensors.[45,46] In most cases, actuation in MEMS is based on electrostatic forces.[45] While commercial MEMS are usually based on silicon technology, several studies explored the fabrication of hybrid MEMS using different types of freestanding nanomaterials. For example, freestanding single-[47] and multi-walled[48] carbon nanotubes have been studied as electrical switches with low pull-in potentials. Other studies reported the application of freestanding graphene sheets as electrostatic resonators.[49] Further, Svensson et al. fabricated a field-effect transistor using suspended graphene gates and demonstrated improved switching behavior with mechanical movement of the gates.[50] Previously, we studied the electrostatic application of membranes from cross-linked gold nanoparticles and their application as sensors for volatile compounds.[6,10,11,18] However, in these membranes the nanoparticles were cross-linked via dithiols, which are prone to oxidation under ambient conditions. Hence, oxidative aging processes can degrade the performance of such devices and limit their operation lifetime. Therefore, the implementation of chemically more robust nanomaterials which in addition feature tunable electrical and mechanical properties, is of significant interest. Addressing this challenge, we turned the initially insulating TNR/GO/SF

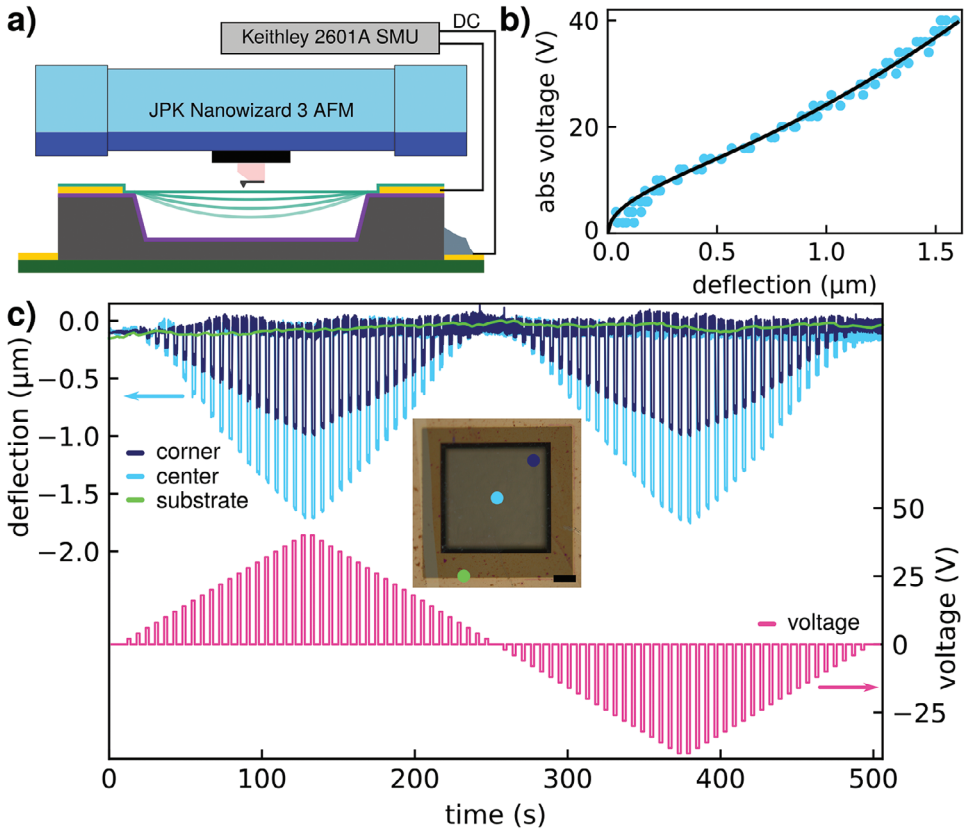

Figure 4. Electrostatic actuation of the TNR/(rGO/GO)/SF membrane. (a) Schematic of the membrane actuator with the AFM used to measure the membrane's deflection. (b) Plot of the voltage-deflection correlation obtained for electrostatically actuated membrane M3. The solid line represents the fit of Equation 5 to the data set within the range of 0.1 to 1.7 µm of deflection. (c) Baseline corrected deflection of the membrane at different positions (blue traces) and corresponding applied bias voltage (red trace). Inset: Optical micrograph of the freestanding membrane spanning a square cavity with edge length of 245 µm and a depth of 21.5 µm. The colored dots mark the position of the deflection measurements. Scale bar: 50 µm.

membranes into conductive TNR/(rGO/GO)/SF membranes by DUV exposure (Figure S5, Supporting Information) and explored their electrostatic actuation. **Figure** 4a shows a schematic drawing of the experimental setup, similar as described in our previous study.[6] The actuators were fabricated by stamping the membrane onto a silicon substrate featuring square cavities with edge lengths of ~245 µm and a depth of ~21.5 µm (cf. Figure S7, Supporting Information).[11] The p-doped silicon substrate served as the bottom electrode while the membrane formed the top electrode. The freestanding section of the membrane and the bottom electrode were separated by the cavity while the remaining sections of the membrane covered a thermally grown silicon oxide layer. Further, the membrane was contacted by a gold electrode which was deposited onto the oxide layer. Before actuation, the membrane was exposed to DUV radiation for 120 min. After the DUV treatment, the thickness of the membrane was ~10 nm (membrane M3, cf. Figure S4, Supporting Information). In order to actuate the membrane, rectangular voltage signals were applied, ranging from –40 to +40 V. At the same time, the resulting deflection of the membrane was measured with an AFM tip operated in intermittent contact mode. When applying the voltage signal the membrane was deflected toward the bottom electrode, independent of the bias polarity (Figure 4c). Further, the deflection increased with increasing absolute voltage. Due to the membrane's elastic behavior the deflection was fully reversible. At each given voltage the deflection value was measured at the centre of the membrane, reaching up to ~1.7 µm at ±40 *V*. As expected, less pronounced deflections were measured when positioning the AFM tip closer to the edge of the freestanding membrane. As a reference measurement, the AFM tip was placed on a substrate-supported section of the membrane. This experiment did not indicate any discernible response of the AFM tip to the applied voltage (cf. Figure 4c).

According to previous studies, the correlation between the applied bias voltage V and the membranes' deflection h can be approximated using Equation (5) (Supporting Information, Section S4):[33,51]

$$\frac{\epsilon V^2}{2d^2} = \frac{8Yt_m}{6(1+\nu)a^4}h^3 + \frac{3.393\sigma_0 t_m}{a^2}h \tag{5}$$

Here, ϵ is approximated by the vacuum permittivity, d is the distance between the membrane and the bottom electrode, t_m is the membrane's thickness, ν is the poisson's ratio (0.33),[34,35] a is half the edge length of the cavity, Y is the biaxial modulus of the membrane, and σ_0 is the prestress. Note, this approximation assumes a simple parallel arrangement of the membrane and the bottom electrode and neglects changes of the electric field due

to the deformation of the actuated membrane. However, for the range of small deflections ($h << d$) and as long as the conditions $h << a$ and $t_m << h$ are fulfilled, this model is expected to provide a useful description of the deflection of the membrane with increasing bias voltage.[33] Figure 4b presents a plot of the applied bias voltage V versus the deflection h of the membrane's central point. A fit to the data according to Equation (5) is shown as solid line. Note, in order to fulfil the condition of small deflections $h << d$ and $t_m << h$ the data used for producing the fit function, were limited to deflections between 0.1 and 1.7 µm. Within this range, the fit function shows good agreement with the data. With the exception of the membrane's prestress all parameters of Equation (5) could be measured and estimated or are known from literature (Supporting Information, Section S4).[52] Hence, the membrane's prestress was extracted as the only free fit parameter, providing a value of ~1.4 MPa. This value is smaller than the prestress values determined by the above-presented AFM bulge tests (Table 1). We assume that this discrepancy results from the different geometry and size of the through holes and the cavity of the substrates used for AFM bulge tests and electrostatic actuation, respectively. The square-root-like shape of the fit function for deflections up to ~1 µm suggests that the behavior of the membrane at small deflections was mainly governed by the membrane's residual stress (second term of Equation 5). Plotting the data on a log/log scale returns a slope of 0.67, confirming that the prestress dominated the membrane's behavior in the range of small deflections (Figure S8, Supporting Information, Section S4). For deflections exceeding 1 µm the first term of Equation (5) becomes more important as indicated by the slight positive curvature of the plotted data and the fit between ~1 and ~1.7 µm.

3. Conclusion

In this study, thin TNR/GO/SF films were prepared using a facile layer-by-layer spin-coating process. These films are fairly robust and can be transfer-printed onto substrates with cavities or through holes to form membranes with freestanding sections of up to ~60 000 µm^2. An interesting feature of these membranes is the tunability of their mechanical and electrical properties which is based on the photocatalytic activity of the TNRs. As shown by AFM and AFM-bulge tests, DUV exposure results in a compaction of the composite material along with an increase of Young's modulus from ~22 GPa to ~35 GPa. This enhancement of the mechanical properties is most likely due to photo-induced cross-linking of the membranes' organic components (GO, SF). The toughness of the irradiated membranes is in the range of 1.25 MJ m^{-3} while the ultimate biaxial tensile stress and strain are in the range of ~377 MPa and ~0.68%, respectively. Furthermore, DUV irradiation lends the initially insulating material electrical conductivity due to the photocatalytic reduction of GO to rGO. Hence, these membranes can be employed as electrostatically driven actuators, which are interesting candidates for applications as sensors and optical devices.[18,46]

In conclusion, the facile tunability of the electrical and mechanical properties of TNR/(GO/rGO)/SF membranes is a great advantage over previously reported hybrid MEMS. Also, compared to previously studied membranes from cross-linked gold nanoparticles,[4,6] these membranes are more robust and feature significantly higher Young's moduli. Further, it should be straightforward to implement additional functional properties by adding other nanomaterials during the facile layer-by-layer fabrication process. For example, by inserting metal or semiconductor nanocrystals, it should be possible to enable additional optical properties. Furthermore, the implementation of magnetic properties should be achievable by inserting magnetic nanocrystals, e.g., magnetite nanocrystals. Using this approach, future works will focus on advancing the membrane's properties for specific applications as sensors and actuators.

4. Experimental Section

Materials: Methanol (≥99.8%), 2-propanol (99.7%), toluene (99.5%), acetone (≥99.8%), chloroform (99%), and hydrochloric acid (37%) were purchased from VWR Chemicals. Hydrogen peroxide (30%), 1-octadecene (ODE, 90%), oleic acid (OLAC, 90%), oleyl amine (OLAM, 98%), and titanium(IV) chloride (99%) were purchased from Merck. Graphite (−325 mesh, 99.8%) and potassium permanganate (99%) were purchased from Alfa Aesar. Silk Fibroin solution (SF, 50 mg/mL ~100 kDa), methoxyperflourobutane (MPFB, ≥99%), and poly methyl methacrylate (PMMA, 120 kDa) were purchased from Sigma-Aldrich. Sulfuric acid (95%) was purchased from Chemsolute. Chlorobenzene (≥99%) was purchased from Burdick Johnson. Polydimethylsiloxane (PDMS, Sylgard 184) was purchased from Dow Corning Inc. Polyvinyl alcohol (PVA, 15 kDa) was purchased from Fluka. All chemicals were used as received without further purification. SiO_2/Si wafers (⟨100⟩, CZ-p-B doped, 8–25 Ω cm, 500 nm wet thermal oxide) were purchased from Siegert Wafer and used for the fabrication of electrostatic actuators. DI water (18.2 MΩ cm) was provided using an ELGA LabWater purification system.

Synthesis of Graphene Oxide and Titania Nanorods: Graphene oxide (GO) was synthesized according to the procedure reported by Hummers et al.[53] with additional purification via dialysis. Titania nanorods (TNRs) were synthesized following the seeded-growth approach reported by Gordon et al.[54] Details of the procedures are described in the Supporting Information, Section S1. Transmission electron microscopy (TEM) was performed to determine the size and the shape of as-synthesized materials. The measurements were conducted using a JEOL JEM-1011 microscope (LaB_6, 100 kV).

Fabrication of Silicon Substrates with Circular Apertures: The circular apertures were fabricated by deep reactive ion etching. The diameters were defined by standard photolithographic techniques. Details of the process can be found in the publication of Hensel et al.[15]

Fabrication of Electrode Structures: Square cavity arrays (depth: ≥21 µm) were etched into silicon substrates using lithographic techniques. The top electrodes were prepared by depositing thin layers of titanium (≥10 nm) and gold (≥40 nm) via thermal evaporation. Hartmann et al. provided detailed instructions on the fabrication process.[11]

Fabrication of Freestanding Hybrid Membranes: The fabrication process has been adapted based on the transfer printing process previously reported by our group.[11] Square pieces (1 × 1 cm^2) of oxidized silicon wafers (Siegert Wafer) were exposed to air plasma (Harrick Plasma Cleaner PDC-002) for 3 min immediately prior to film deposition. The substrates were constantly rotated at 3000 rpm using a Karl Suess LabSpin 6TT spin-coater. Initially, 100 µL of a 25 mg mL^{-1} aqueous PVA solution were deposited onto the substrate. After 100 s, 2 × 25 µL of GO dispersion (0.4 mg mL^{-1} dispersed in a 1:1 mixture of methanol and DI water) were deposited followed by the deposition of 3 × 25 µL of an aqueous solution of SF (2 mg mL^{-1}). Afterwards, 1 × 25 µL of GO dispersion and 1 × 25 µL of SF solution were deposited, followed by 3 × 25 µL of GO dispersion, 1 × 25 µL of a TNR dispersion (0.5 mg mL^{-1} in chloroform) and 2 × 25 µL of GO dispersion. All deposition steps were seperated by delays of 25 s. The obtained film was divided into four sections (~3 × 3 mm^2) using a scalpel to remove the film at the margins and in the centre. The films were reinforced for the following transfer step by depositing 70 µL of a PMMA solution (50 mg mL^{-1} in chlorobenzene) while the substrate was rotated

at 3000 rpm for 100 s. The coated substrate was then baked on a hot plate (Harry Gestigkeit Präzitherm 2860SR) at 60 °C for 10 min. The layer stack was divided into four sections using a scalpel. Each section of the hybrid film was transferred individually. The section was covered with 15 µL DI water. A rectangular PDMS stamp (10/1, m/m, oligomeric base to curing agent; ~5 × 6 × 1.6 mm^3) was pressed against the substrate at a pressure of 0.26 bar for 5 s. When removing the stamp, the hybrid film was transferred to the PDMS stamp. The target substrates were exposed to air plasma for 3 min. The stamp with the hybrid film was pressed against the substrate at a pressure of 1.8 bar. Following the method reported by Choi et al.,[30] the hybrid film was detached from the stamp and transferred to the target substrate by applying three cycles of heating the structure to 70 °C and cooling it down to −3 °C using thermoelectric cooling under nitrogen flow. Each temperature was maintained for 6 min. Afterwards, the stamp was lifted off and the substrate with the composite film was transferred into a PTFE container. The protective PMMA layer on the transferred film was then dissolved in acetone. Finally, the acetone was exchanged for MPFB which has a lower surface tension than acetone. Therefore, MPFB reduces drag forces acting on the freestanding membranes when removing the substrate from the liquid phase and when drying the sample at ambient conditions.[31]

The morphology and thickness of the films were characterized by optical microscopy (Olympus BX51 with UC30 CCD camera), scanning electron microscopy (SEM, Zeiss LEO-1550 Gemini) and atomic force microscopy (AFM, JPK NanoWizard 3).

DUV Treatment: The hybrid films with the freestanding membrane sections were exposed to deep-UV (DUV) radiation for 80–120 min using a custom-built DUV light source[55] with a main emission peak at 254 nm. The irradiance on the sample surface was ~520 mW cm^{-2}, which was determined using a Thorlabs PM100 powermeter, equipped with a Thorlabs S120 UV sensor. To prevent heating of the samples the housing of the setup was ventilated by an electrical fan.

Bulge Tests: Prior to the bulge tests, the thickness of the membranes and the radius of the circular freestanding membrane sections were determined by AFM and optical microscopy, respectively. The bulge tests were conducted using the same experimental setup and methods as described in detail in our previous studies.[4,15,17,33] The holey substrates with freestanding membranes were fixed onto custom-built sample holders using double-sided sticky tape (Tesa 05338). Topographic data were acquired using an AFM (JPK Nanowizard 3) equipped with NSG01 cantilevers. Ten evenly spaced line scans of 512 pixels within the total scan area of 100 × 100 $µm^2$ were performed using the intermittent contact mode. The lateral scan range was chosen to cover major parts of the freestanding membrane and sections of the substrate. Negative differential pressures in the range between 0.1 kPa and 6 kPa were applied to the membranes in ascending and descending order. The increments were 100 Pa between 0.1 and 1.0 kPa, 200 Pa between 1 and 3 kPa, and 300 Pa between 3 and 6 kPa. The same increments in the respective pressure ranges were applied for descending the pressure from 6 kPa to 0.1 kPa. For burst experiments, the increments to 6 kPa were kept the same, but they were increased to 1 kPa between 6 and 10 kPa, 2 kPa between 10 and 40 kPa and reduced again to 1 kPa between 40 and 85 kPa. The pressure was controlled using three pressure gauges (Sensortechnics, HDIB001DBF8P5 -100–100kPa, HDIM100DUF8P5 0–10kPa, HDIM010DUF8P5 0–1kPa). Data of the AFM bulge tests were evaluated using the spherical cap model of a thin-walled pressure vessel.[15,17,52]

Actuator Tests: The actuator tests were performed with the same setup described in our previous study using an AFM (JPK Nanowizard 3 equipped with ACTA-50 cantilevers) to detect the deflection of the hybrid membrane.[6] The AFM was operated in intermittent contact mode, and the deflection was measured as a function of time at fixed x,y-coordinates. Voltages of up to ±40 V were applied to the membrane with incremental step sizes of 2 V using a Keithley 2601A source measure unit. Each voltage was maintained for 2 s followed by 4 s at 0 V. The actuator tests were repeated to measure the membrane's deflection at different positions on the freestanding membrane.

Supporting Information

Supporting Information is available from the Wiley Online Library or from the author.

Acknowledgements

The authors acknowledge financial support from the Open Access Publication Fund of Universität Hamburg. The authors thank the electron microscopy service unit, especially Robert Schön and Stefan Werner, for SEM and TEM data. Gefördert durch die Deutsche Forschungsgemeinschaft (DFG) - 395896547; 408076438. Funded by the Deutsche Forschungsgemeinschaft (DFG, German Research Foundation) - 395896547; 408076438.

Conflict of Interest

The authors declare no conflict of interest.

Author Contributions

H.H., F.D., and T.V. proposed and developed the research idea. F.D., H.H., and H.S. did the experimental design for film transfer, bulge tests, and electrostatic actuation. Major parts of the experimental work and data analysis were carried out by F.D. The titania nanorods and the graphene oxide were synthesised by S.C.B. and H.H., respectively. H.H. prepared the electrostatically driven actuator. The through hole substrates were fabricated by N.S. and H.K.T. Data evaluation and manuscript writing were done by F.D. and T.V. The project was supervised by T.V.

Data Availability Statement

The data that support the findings of this study are available from the corresponding author upon reasonable request.

Keywords

actuator, graphene, stiffness, titania, toughness

Received: August 1, 2024
Revised: October 24, 2024
Published online:

[1] T. Yildirim, L. Zhang, G. P. Neupane, S. Chen, J. Zhang, H. Yan, M. M. Hasan, G. Yoshikawa, Y. Lu, *Nanoscale* **2020**, *12*, 22366.
[2] Q. Shi, W. Cheng, *Adv. Funct. Mater.* **2020**, *30*, 1902301.
[3] M. Chen, W. Luo, Z. Xu, X. Zhang, B. Xie, G. Wang, M. Han, *Nat. Commun.* **2019**, *10*, 4024.
[4] H. Schlicke, S. Kunze, M. Rebber, N. Schulz, S. Riekeberg, H. K. Trieu, T. Vossmeyer, *Adv. Funct. Mater.* **2020**, *30*, 2003381.
[5] M. Kandpal, C. Sharan, V. Palaparthy, N. Tiwary, P. Poddar, V. R. Rao, *RSC Adv.* **2015**, *5*, 85741.
[6] H. Schlicke, D. Battista, S. Kunze, C. J. Schröter, M. Eich, T. Vossmeyer, *ACS Appl. Mater. Interfaces* **2015**, *7*, 15123.
[7] A. U. Khan, G. Zeltzer, G. Speyer, Z. L. Croft, Y. Guo, Y. Nagar, V. Artel, A. Levi, C. Stern, D. Naveh, G. Liu, *Adv. Mater.* **2021**, *33*, 2004053.

[8] H. Schlicke, C. J. Schröter, T. Vossmeyer, *Nanoscale* **2016**, *8*, 15880.
[9] H. Guo, L. Lou, X. Chen, C. Lee, *IEEE Electron Device Lett.* **2012**, *33*, 1078.
[10] H. Schlicke, M. Behrens, C. J. Schröter, G. T. Dahl, H. Hartmann, T. Vossmeyer, *ACS Sensors* **2017**, *2*, 540.
[11] H. Hartmann, J.-N. Beyer, J. Hansen, S. C. Bittinger, M. Yesilmen, H. Schlicke, T. Vossmeyer, *ACS Appl. Mater. Interfaces* **2021**, *13*, 40932.
[12] M. I. Dafinone, G. Feng, T. Brugarolas, K. E. Tettey, D. Lee, *ACS Nano* **2011**, *5*, 5078.
[13] K. E. Mueggenburg, X.-M. Lin, R. H. Goldsmith, H. M. Jaeger, *Nat. Mater.* **2007**, *6*, 656.
[14] A. Turchanin, A. Beyer, C. T. Nottbohm, X. Zhang, R. Stosch, A. Sologubenko, J. Mayer, P. Hinze, T. Weimann, A. Gölzhäuser, *Adv. Mater.* **2009**, *21*, 1233.
[15] A. Hensel, C. J. Schröter, H. Schlicke, N. Schulz, S. Riekeberg, H. K. Trieu, A. Stierle, H. Noei, H. Weller, T. Vossmeyer, *Nanomaterials* **2019**, *9*, 1230.
[16] S. Markutsya, C. Jiang, Y. Pikus, V. V. Tsukruk, *Adv. Funct. Mater.* **2005**, *15*, 771.
[17] H. Schlicke, S. Kunze, M. Finsel, E. W. Leib, C. J. Schröter, M. Blankenburg, H. Noei, T. Vossmeyer, *J. Phys. Chem. C* **2019**, *123*, 19165.
[18] H. Schlicke, M. Rebber, S. Kunze, T. Vossmeyer, *Nanoscale* **2016**, *8*, 183.
[19] R. J. Nicholl, H. J. Conley, N. V. Lavrik, I. Vlassiouk, Y. S. Puzyrev, V. P. Sreenivas, S. T. Pantelides, K. I. Bolotin, *Nat. Commun.* **2015**, *6*, 8789.
[20] Y. Wang, R. Ma, K. Hu, S. Kim, G. Fang, Z. Shao, V. V. Tsukruk, *ACS Appl. Mater. Interfaces* **2016**, *8*, 24962.
[21] R. Xiong, K. Hu, A. M. Grant, R. Ma, W. Xu, C. Lu, X. Zhang, V. V. Tsukruk, *Adv. Mater.* **2016**, *28*, 1501.
[22] K. Hu, M. K. Gupta, D. D. Kulkarni, V. V. Tsukruk, *Adv. Mater.* **2013**, *25*, 2301.
[23] K. Sellschopp, W. Heckel, J. Gäding, C. J. Schröter, A. Hensel, T. Vossmeyer, H. Weller, S. Müller, G. B. Vonbun-Feldbauer, *J. Chem. Phys.* **2020**, *152*, 064702.
[24] B. Li, X. Zhang, X. Li, L. Wang, R. Han, B. Liu, W. Zheng, X. Li, Y. Liu, *Chem. Commun.* **2010**, *46*, 3499.
[25] M. Hada, K. Miyata, S. Ohmura, Y. Arashida, K. Ichiyanagi, I. Katayama, T. Suzuki, W. Chen, S. Mizote, T. Sawa, T. Yokoya, T. Seki, J. Matsuo, T. Tokunaga, C. Itoh, K. Tsuruta, R. Fukaya, S. Nozawa, S.-i. Adachi, J. Takeda, K. Onda, S.-y. Koshihara, Y. Hayashi, Y. Nishina, *ACS Nano* **2019**, *13*, 10103.
[26] G. Williams, B. Seger, P. V. Kamat, *ACS Nano* **2008**, *2*, 1487.
[27] H. Zhang, X. Lv, Y. Li, Y. Wang, J. Li, *ACS Nano* **2010**, *4*, 380.
[28] S. J. Hug, D. Bahnemann, *J. Electron Spectrosc. Relat. Phenom.* **2006**, *150*, 208.
[29] S. Ayissi, P. A. Charpentier, N. Farhangi, J. A. Wood, K. Palotás, W. A. Hofer, *J. Phys. Chem. C* **2013**, *117*, 25424.
[30] M. K. Choi, I. Park, D. C. Kim, E. Joh, O. K. Park, J. Kim, M. Kim, C. Choi, J. Yang, K. W. Cho, J. Hwang, J. Nam, T. Hyeon, J. H. Kim, D. Kim, *Adv. Funct. Mater.* **2015**, *25*, 7109.
[31] Y.-M. Chen, S.-M. He, C.-H. Huang, C.-C. Huang, W.-P. Shih, C.-L. Chu, J. Kong, J. Li, C.-Y. Su, *Nanoscale* **2016**, *8*, 3555.
[32] E. Schweitzer, M. Göken, *J. Mater. Res.* **2007**, *22*, 2902.
[33] H. Schlicke, E. W. Leib, A. Petrov, J. H. Schröder, T. Vossmeyer, *J. Phys. Chem. C* **2014**, *118*, 4386.
[34] P. Podsiadlo, G. Krylova, B. Lee, K. Critchley, D. J. Gosztola, D. V. Talapin, P. D. Ashby, E. V. Shevchenko, *J. Am. Chem. Soc.* **2010**, *132*, 8953.
[35] J. He, P. Kanjanaboos, N. L. Frazer, A. Weis, X.-M. Lin, H. M. Jaeger, *Small* **2010**, *6*, 1449.
[36] H. Cho, J. Lee, H. Hwang, W. Hwang, J.-G. Kim, S. Kim, *Friction* **2022**, *10*, 282.
[37] J. W. Suk, R. D. Piner, J. An, R. S. Ruoff, *ACS Nano* **2010**, *4*, 6557.
[38] C. Jiang, X. Wang, R. Gunawidjaja, Y.-H. Lin, M. Gupta, D. Kaplan, R. Naik, V. Tsukruk, *Adv. Funct. Mater.* **2007**, *17*, 2229.
[39] S. Keten, Z. Xu, B. Ihle, M. J. Buehler, *Nat. Mater.* **2010**, *9*, 359.
[40] J. Soria, M. López-Muñoz, V. Augugliaro, J. Conesa, *Colloids Surf., A* **1993**, *78*, 73.
[41] V. Bellotti, C. Daldossi, D. Perilli, M. D'Arienzo, M. Stredansky, C. Di Valentin, R. Simonutti, *J. Catal.* **2023**, *428*, 115074.
[42] T. Tanaka, S. Nishimura, K. Nishiyama, Y. Aso, H. Nishida, S. Cho, T. Sekino, *Asian J. Org. Chem.* **2024**, 202400270.
[43] X. Wang, Q. Lu, X. Wang, J. Joo, M. Dahl, B. Liu, C. Gao, Y. Yin, *ACS Appl. Mater. Interfaces* **2016**, *8*, 538.
[44] K. Hu, L. S. Tolentino, D. D. Kulkarni, C. Ye, S. Kumar, V. V. Tsukruk, *Angew. Chem.* **2013**, *125*, 14029.
[45] J. G. Noel, *IET Circuits, Devices & Systems* **2016**, *10*, 156.
[46] J. Li, J. A. Hutchison, D. Smith, H. Wu, P. Mulvaney, *Nano Lett.* **2024**, *24*, 4362.
[47] A. B. Kaul, E. W. Wong, L. Epp, B. D. Hunt, *Nano Lett.* **2006**, *6*, 942.
[48] A. Subramanian, A. R. Alt, L. Dong, B. E. Kratochvil, C. R. Bolognesi, B. J. Nelson, *ACS Nano* **2009**, *3*, 2953.
[49] A. Castellanos-Gomez, V. Singh, H. S. J. Van Der Zant, G. A. Steele, *Ann. Phys.* **2015**, *527*, 27.
[50] J. Svensson, N. Lindahl, H. Yun, M. Seo, D. Midtvedt, Y. Tarakanov, N. Lindvall, O. Nerushev, J. Kinaret, S. Lee, E. E. B. Campbell, *Nano Lett.* **2011**, *11*, 3569.
[51] J. Vlassak, W. Nix, *J. Mater. Res.* **1992**, *7*, 3242.
[52] M. K. Small, W. Nix, *J. Mater. Res.* **1992**, *7*, 1553.
[53] W. S. Hummers, R. E. Offeman, *J. Am. Chem. Soc.* **1958**, *80*, 1339.
[54] T. R. Gordon, M. Cargnello, T. Paik, F. Mangolini, R. T. Weber, P. Fornasiero, C. B. Murray, *J. Am. Chem. Soc.* **2012**, *134*, 6751.
[55] H. Schlicke, S. C. Bittinger, T. Vossmeyer, *ACS Appl. Electron. Mater.* **2020**, *2*, 3741.